

LETTER TO THE EDITOR

# Surveying the Whirlpool at Arcseconds with NOEMA (SWAN)

## I. Mapping the HCN and N<sub>2</sub>H<sup>+</sup> 3mm lines

Sophia K. Stuber<sup>1</sup>, Jerome Pety<sup>2,3</sup>, Eva Schinnerer<sup>1</sup>, Frank Bigiel<sup>4</sup>, Antonio Usero<sup>5</sup>, Ivana Bešlić<sup>3</sup>, Miguel Querejeta<sup>5</sup>,  
María J. Jiménez-Donaire<sup>5,6</sup>, Adam Leroy<sup>7</sup>, Jakob den Brok<sup>8</sup>, Lukas Neumann<sup>4</sup>, Cosima Eibensteiner<sup>4</sup>, Yu-Hsuan  
Teng<sup>9</sup>, Ashley Barnes<sup>10</sup>, Mélanie Chevance<sup>11,12</sup>, Dario Colombo<sup>4</sup>, Daniel A. Dale<sup>13</sup>, Simon C. O. Glover<sup>11</sup>, Daizhong  
Liu<sup>14</sup>, and Hsi-An Pan<sup>15</sup>

(Affiliations can be found after the references)

Accepted November 30, 2023

### ABSTRACT

We present the first results from "Surveying the Whirlpool at Arcseconds with NOEMA" (SWAN), an IRAM Northern Extended Millimetre Array (NOEMA)+30m large program that maps emission from several molecular lines at 90 and 110 GHz in the iconic nearby grand-design spiral galaxy M 51 at cloud-scale resolution ( $\sim 3'' = 125$  pc). As part of this work, we have obtained the first sensitive cloud-scale map of N<sub>2</sub>H<sup>+</sup> (1-0) of the inner  $\sim 5 \times 7$  kpc of a normal star-forming galaxy, which we compare to HCN (1-0) and <sup>12</sup>CO (1-0) emission to test their ability in tracing dense, star-forming gas. The average N<sub>2</sub>H<sup>+</sup>-to-HCN line ratio of our total FoV is  $0.20 \pm 0.09$ , with strong regional variations of a factor of  $\geq 2$  throughout the disk, including the south-western spiral arm and the center. The central  $\sim 1$  kpc exhibits elevated HCN emission compared to N<sub>2</sub>H<sup>+</sup>, probably caused by AGN-driven excitation effects. We find that HCN and N<sub>2</sub>H<sup>+</sup> are strongly super-linearly correlated in intensity ( $\rho_{sp} \sim 0.8$ ), with an average scatter of  $\sim 0.14$  dex over a span of  $\geq 1.5$  dex in intensity. When excluding the central region, the data is best described by a power-law of exponent 1.2, indicating that there is more N<sub>2</sub>H<sup>+</sup> per unit HCN in brighter regions. Our observations demonstrate that the HCN-to-CO line ratio is a sensitive tracer of gas density in agreement with findings of recent Galactic studies which utilize N<sub>2</sub>H<sup>+</sup>. The peculiar line ratios present near the AGN and the scatter of the power-law fit in the disk suggest that in addition to a first-order correlation with gas density, second-order physics (such as optical depth, gas temperature) or chemistry (abundance variations) are encoded in the N<sub>2</sub>H<sup>+</sup>/<sup>12</sup>CO, HCN/<sup>12</sup>CO and N<sub>2</sub>H<sup>+</sup>/HCN ratios.

**Key words.** ISM:molecules - galaxies:ISM - galaxies: individual: M51

### 1. Introduction

The emission lines of molecules such as <sup>12</sup>CO are considered good tracers of the bulk molecular mass distribution (e.g., BIMA-SONG, Helfer et al. 2003; PAWS, Schinnerer et al. 2013; PHANGS, Leroy et al. 2021), and are found to correlate with (e.g., infrared) emission tracing recent star formation (e.g., Kennicutt & Evans 2012; Bigiel et al. 2008). However, molecular clouds contain a wide range of densities, with star formation typically associated with the densest gas (e.g., Lada et al. 2010, 2012). Extragalactic studies show that CO emission does not distinguish between lower density, bulk molecular gas and the star-forming, dense material with H<sub>2</sub> densities of  $\geq 10^4$  cm<sup>-3</sup> (e.g., Gao & Solomon 2004; Jiménez-Donaire et al. 2019; Querejeta et al. 2019)

Tracers of dense gas are by definition challenging to observe due to the lower abundances of these molecules relative to CO and the smaller volume occupied by the dense phase, which both lead to a much reduced line brightness when compared to CO. With typical HCN-to-CO line ratios in disk galaxies of  $\sim 1/30$  or lower (Usero et al. 2015; Bigiel et al. 2016), extragalactic studies were focusing on HCN (J=1-0) finding a tighter correlation between HCN line emission with star formation rate (SFR) than for CO emission (Gao & Solomon 2004; Jiménez-Donaire et al. 2019). The higher critical density ( $n_{crit}$ ) of HCN (1-0) has led to the common interpretation that this line preferentially traces the denser sub-regions of molecular clouds (Shirley 2015) making HCN a commonly used tracer of dense molecular gas in

extragalactic studies (Bigiel et al. 2016; Gallagher et al. 2018; Jiménez-Donaire et al. 2019; Querejeta et al. 2019; Bešlić et al. 2021; Eibensteiner et al. 2022; Neumann et al. 2023; Kaneko et al. 2023).

Galactic studies have questioned the use of HCN as a dense gas tracer at cloud scales ( $< 10$  pc) and favour the use of another molecule, N<sub>2</sub>H<sup>+</sup>, which has successfully been detected towards several molecular clouds in the Milky Way (e.g., Pety et al. 2017; Kauffmann et al. 2017; Barnes et al. 2020; Tafalla et al. 2021; Beuther et al. 2022; Santa-Maria et al. 2023; Tafalla et al. 2023). Since N<sub>2</sub>H<sup>+</sup> is destroyed in the presence of CO, it is linked to the dense clumps of clouds, where CO freezes to dust grains (e.g., Bergin & Tafalla 2007). This makes N<sub>2</sub>H<sup>+</sup> not only a chemical tracer of cold and dense cores within clouds, but also leads to its emission being beam-diluted and thus even fainter than HCN (e.g., N<sub>2</sub>H<sup>+</sup>/<sup>12</sup>CO  $\sim 1/100$  at  $\sim 150$  pc scales in a starburst galaxy; Eibensteiner et al. 2022, N<sub>2</sub>H<sup>+</sup>/<sup>12</sup>CO  $\sim 1/140$  at kpc scales in M 51 den Brok et al. 2022). Extragalactic observations of N<sub>2</sub>H<sup>+</sup> are thus challenging and limited to low-resolution studies (e.g.,  $\sim$ kpc scales; den Brok et al. 2022; Jiménez-Donaire et al. 2023) or individual regions of galaxies (e.g., the center of starburst galaxy NGC 253; Martín et al. 2021). Jiménez-Donaire et al. (2023) summarize Galactic and extragalactic observations of HCN and N<sub>2</sub>H<sup>+</sup>. Although challenging, the IRAM Northern Extended Millimetre Array (NOEMA) is capable of obtaining high sensitivity and high angular resolution observations needed to map the distribution of the faint emission of N<sub>2</sub>H<sup>+</sup> and HCN in star-forming galaxy disks.

We present the first results from the SWAN (Surveying the Whirlpool at Arcsecond with NOEMA) IRAM Large Program (PIs: E. Schinnerer & F. Bigiel), including the first cloud-scale (125 pc) extragalactic map of  $\text{N}_2\text{H}^+$  in the central 5–7 kpc of the Whirlpool galaxy, a.k.a M 51. SWAN targets nine molecular lines ( $\text{C}_2\text{H}(1-0)$ ,  $\text{HNCO}(4-3)$ ,  $\text{HCN}(1-0)$ ,  $\text{HCO}^+(1-0)$ ,  $\text{HNC}(1-0)$ ,  $\text{N}_2\text{H}^+(1-0)$ ,  $\text{C}^{18}\text{O}(1-0)$ ,  $\text{HNCO}(5-4)$ ,  $^{13}\text{CO}(1-0)$ ) at  $\sim 3''$  ( $\sim 125$  pc) to study the role of dense gas in the star formation process across galactic environments.

M 51 (NGC 5194) is a nearby ( $D = 8.58$  Mpc; McQuinn et al. 2016) close to face-on ( $i = 22^\circ$ , P.A. =  $173^\circ$ ; Colombo et al. 2014) massive ( $\log_{10} M_*/M_\odot = 10.5$ ; den Brok et al. 2022) spiral galaxy that hosts a low-luminosity AGN (Ho et al. 1997; Dumas et al. 2011; Querejeta et al. 2016). HCN has been mapped at  $3''$  resolution (125 pc) for three circular regions of  $\sim 3$  kpc diameter (Querejeta et al. 2019) in M 51, at  $4''$  in the outer spiral arm at  $\sim 5$  kpc galactocentric distance (Chen et al. 2017) and out to  $\sim 8$  kpc in the disk at 1–2 kpc resolution by EMPIRE (Bigiel et al. 2016; Jiménez-Donaire et al. 2019). Watanabe et al. (2014) detected both HCN and  $\text{N}_2\text{H}^+(1-0)$  at  $\sim$ kpc resolution in two 30m pointings in the south-western spiral arm, and den Brok et al. (2022) presented  $\text{N}_2\text{H}^+$  observations of its center at  $\sim$ kpc resolution.

Sec. 2 describes our observations and data reduction, followed by a comparison of the  $\text{N}_2\text{H}^+$ , HCN, and CO line emission in Sec. 3, a discussion in Sec. 4 and a summary (Sec. 5).

## 2. Data

We use observations from the IRAM large program LP003 (PIs: E. Schinnerer, F. Bigiel) that combines NOEMA (integration time of  $\sim 214$ h) and the 30m single dish observations (about  $\sim 69$ h integration time from EMPIRE, CLAWS, and this program) to map 3–4 mm emission lines from the central  $5 \times 7$  kpc of the nearby galaxy M 51. A detailed description of the observations and data reduction is presented in Appendix A.

The combined data as well as  $^{12}\text{CO}$  data from PAWS (Schinnerer et al. 2013) are smoothed to a common angular and spectral resolution of  $3''$  and 10 km/s per channel. We integrate each line by applying the so-called GILDAS-based *island-method* (see Einig et al. 2023, and references therein), where structures with  $^{12}\text{CO}$  emission above a selected S/N of 2 in the position-position-velocity cube are selected. For all lines, the emission is then integrated over the same pixels from the  $^{12}\text{CO}$ -based 3D-mask.

## 3. Results on dense gas in M 51

Our SWAN observations have imaged the line emission of both HCN(1-0) (hereafter HCN) and  $\text{N}_2\text{H}^+(1-0)$  (hereafter  $\text{N}_2\text{H}^+$ ) in M 51 at 125 pc resolution. In order to analyze which physical conditions might impact the brightness of these potential dense molecular gas tracers, we study the  $\text{N}_2\text{H}^+$ -to-HCN ratio across the disk of M 51 (Sec. 3.1), identify regions where the ratio deviates from the global trend (3.2), and quantify the correlation between  $\text{N}_2\text{H}^+$  and HCN emission (Sec. 3.3).

### 3.1. Distribution of $\text{N}_2\text{H}^+$ and HCN in the disk of M 51

Figure 1 shows the integrated intensity maps of HCN(1-0) and  $\text{N}_2\text{H}^+(1-0)$ , their ratio (upper panels), and the PAWS  $^{12}\text{CO}(1-0)$  map (bottom left). For five beam-sized  $\text{N}_2\text{H}^+$ -bright regions in the disk (see  $^{12}\text{CO}$  map) we extract average spectra of HCN,

**Table 1.** Typical line ratios of  $\text{N}_2\text{H}^+$ , HCN and  $^{12}\text{CO}$  in M 51

Line ratio	Average $\pm$ sdev
$\text{N}_2\text{H}^+/\text{HCN}(1-0)$	$0.20 \pm 0.09$
$\text{N}_2\text{H}^+/\text{HCN}$ center	$0.15 \pm 0.05$
$\text{N}_2\text{H}^+/\text{HCN}$ disk	$0.24 \pm 0.26$
<i><math>\text{N}_2\text{H}^+/\text{HCN}</math> in beam-size regions:</i>	
region 1 (nucleus)	$0.08 \pm 0.04$
region 2	$0.33 \pm 0.06$
region 3	$0.28 \pm 0.07$
region 4	$0.23 \pm 0.03$
region 5	$0.24 \pm 0.04$
$\text{HCN}/\text{CO}(1-0)$	$0.05 \pm 0.04$
$\text{HCN}/^{12}\text{CO}$ center	$0.10 \pm 0.07$
$\text{HCN}/^{12}\text{CO}$ disk	$0.04 \pm 0.02$
$\text{N}_2\text{H}^+/\text{CO}(1-0)$	$0.012 \pm 0.006$
$\text{N}_2\text{H}^+/\text{CO}$ center	$0.015 \pm 0.007$
$\text{N}_2\text{H}^+/\text{CO}$ disk	$0.011 \pm 0.005$

**Notes.** Average line ratios of  $\text{N}_2\text{H}^+$ -to-HCN as well as HCN-to- $^{12}\text{CO}$  and  $\text{N}_2\text{H}^+$ -to- $^{12}\text{CO}$  for regions with both HCN and  $\text{N}_2\text{H}^+$  emission  $> 3\sigma$  (see Figure 1). We list values for the full FoV, as well as for the central 1.5 kpc in diameter (center) and the remaining disk. For the  $\text{N}_2\text{H}^+$ -to-HCN ratio we further provide ratios of five  $\text{N}_2\text{H}^+$ -bright beam-sized regions in the disk selected visually (compare Fig. 1). The uncertainty is the standard deviation.

$\text{N}_2\text{H}^+$ , and  $^{12}\text{CO}$  (bottom middle panel).  $\text{N}_2\text{H}^+$  emission is detected from various extended regions in the disk, including both spiral arms, the molecular ring and interarm regions. Both tracers ( $\text{N}_2\text{H}^+$ , HCN) roughly follow the CO brightness distribution with the brightest regions being the galaxy center (denoted as region 1), the southwestern spiral arm (2), as well as the north-western part of the inner molecular ring (4).

On average,  $\text{N}_2\text{H}^+$  is  $\sim 5$  times fainter than HCN, and  $\sim 80$  times fainter than CO, while line profiles are very similar (FWHM for  $\text{N}_2\text{H}^+$ :  $\sim 20$  km/s, HCN  $\sim 30$  km/s)<sup>1</sup>, in agreement with  $\sim$ kpc observations in NGC 6946 (Jiménez-Donaire et al. 2023). This remains true, even when imaging our data at 1 km/s spectral resolution. As observations of  $\sim 0.1$  pc  $\text{N}_2\text{H}^+$  clumps in the Milky Way suggest a factor of  $\sim 10$  smaller  $\text{N}_2\text{H}^+$  linewidths relative to HCN (e.g., 1–2 km/s; Tatematsu et al. 2008), our linewidths probably trace cloud-to-cloud velocity dispersion or turbulence scaling with physical lengths. Further, the typical  $^{12}\text{CO}$  luminosity measured per beam (for details see Appendix B) indicates multiple clouds per beam. We conclude that the similar HCN and  $\text{N}_2\text{H}^+$  linewidths suggest that HCN and  $\text{N}_2\text{H}^+$  spatially coexist inside GMCs at these  $> 100$  pc scales and only differ at scales below our resolution.

### 3.2. $\text{N}_2\text{H}^+$ -to-HCN line ratios

Our average  $\text{N}_2\text{H}^+$ -to-HCN ratio is  $\sim 0.20 \pm 0.09$  (see Table 1) in regions with detected  $\text{N}_2\text{H}^+$  emission ( $> 3\sigma$ ) in the integrated intensity map. Table 1 lists average  $\text{N}_2\text{H}^+/\text{HCN}$ ,  $\text{N}_2\text{H}^+/\text{CO}$  and  $\text{HCN}/^{12}\text{CO}$  ratios derived for the full FoV, the central 1.5 kpc in diameter, as well as the remaining disk<sup>2</sup>. The size of the cen-

<sup>1</sup>When considering Gaussian line profiles and that HCN is on average  $\sim 5$  times brighter than  $\text{N}_2\text{H}^+$ , the inferred linewidths at matched brightness agree for HCN and  $\text{N}_2\text{H}^+$ .

<sup>2</sup>The maps are regridded to  $1.5''$  pixel size to minimize oversampling effects.

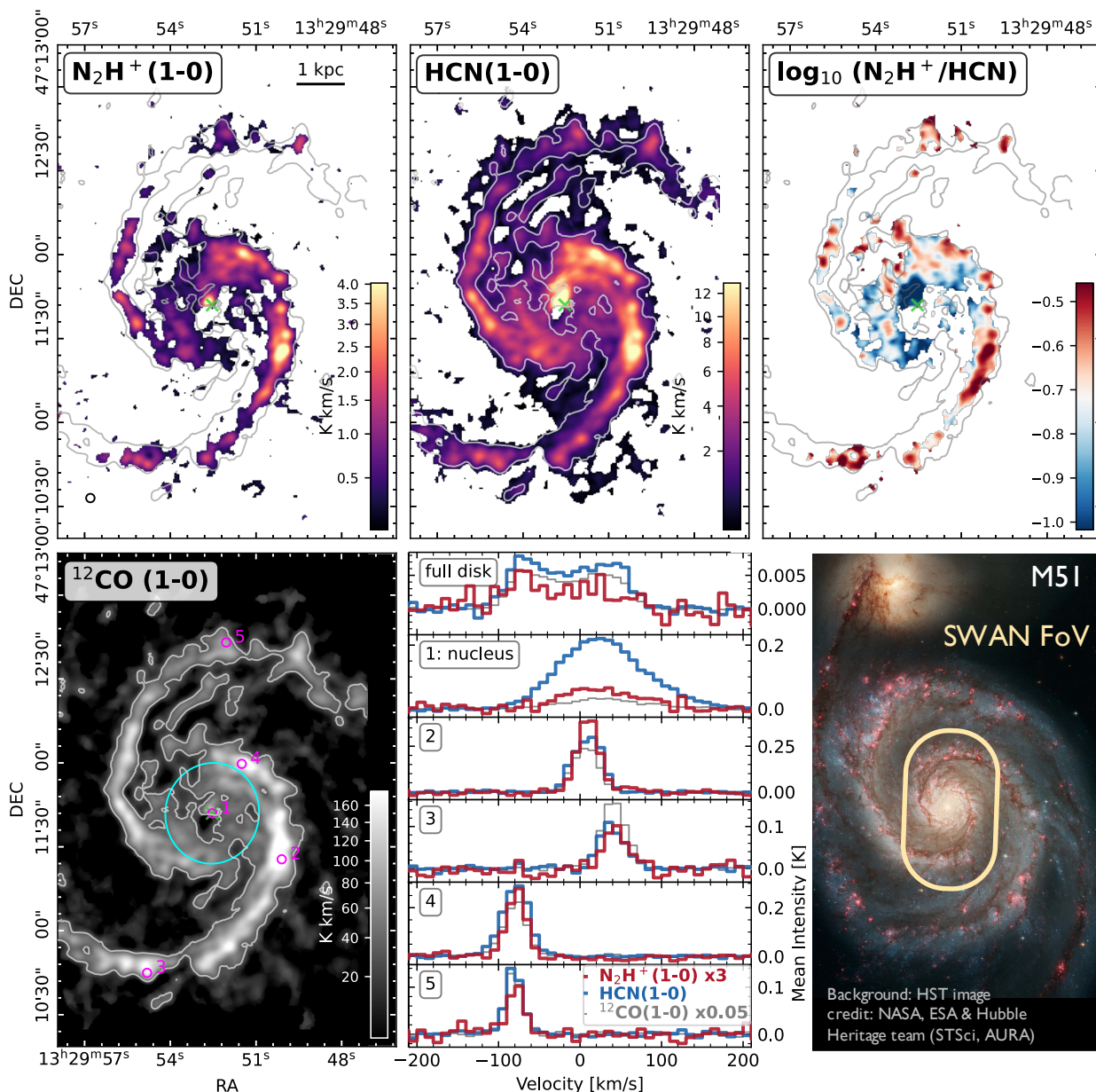


**Fig. 1.** Integrated intensity maps of  $N_2H^+$  (top left) and HCN (top center), as well as their ratio (top right) at  $3''$  ( $\sim 125$  pc) resolution of the central  $5 \text{ kpc} \times 7 \text{ kpc}$  in M 51a. The ratio map shows emission above  $3\sigma$  for both lines. The beam of  $\sim 3''$  is shown in the bottom left corner of the  $N_2H^+$  map for reference; the location of the galactic center is marked (green  $\times$ ). We further display  $^{12}CO$  emission at  $3''$  resolution from the PAWS survey (bottom left; Schinnerer et al. 2013) for comparison and show the  $30 \text{ K km/s}$  contour of  $^{12}CO$  for reference in all maps. The central  $1.5 \text{ kpc}$  (in diameter) is indicated by a cyan circle in the  $^{12}CO$  map. Average spectra of five beam-sized regions in the disk (see the  $^{12}CO$  map) are shown for  $N_2H^+$ , HCN and  $^{12}CO$  (bottom center). We scale the spectra by a factor of 3 ( $N_2H^+$ ) and 0.05 ( $^{12}CO$ ) for easier comparison. The full-disk spectra contain all pixels in the FoV, shown on top of a HST image (bottom right).

tral region is visually set to conservatively encapsulate the area surrounding the center, where low  $N_2H^+$ -to-HCN ratios are observed (see Fig. 1), but not to include other morphological structures such as the molecular ring at larger radii. For these  $\geq 1 \text{ kpc}$  regions, the  $N_2H^+$ -to-HCN line ratio in the center (disk) is lower (higher) by a factor  $\sim 1.3$  ( $\sim 1.2$ ) compared to the full FoV value, but still agrees within the uncertainties.

On  $\sim$ cloud-size scales ( $125 \text{ pc}$ ), the  $N_2H^+$ -to-HCN ratio is significantly ( $> 3\sigma$ ) lower in the center (1) than in region 2 in the south-western spiral arm (see Fig. 1 & Table 1) and deviates by a factor of 2.5 from the full FoV average. These findings suggest

the presence of systematic trends that drive the high scatter of the full FoV line ratios (see next section).

### 3.3. Correlation of HCN and $N_2H^+$ line emission

To study how well the  $N_2H^+$  and HCN emission correlate, we analyze the pixel-by-pixel distribution of  $N_2H^+$  intensity as a function of HCN intensity<sup>2</sup> (Fig. 2, for  $N_2H^+$  and HCN as a function of  $^{12}CO$  emission see Appendix C).

To first order, the  $N_2H^+$  emission is strongly correlated with the HCN emission (Spearman correlation coefficient  $\rho_{\text{Sp}} = 0.832 \pm 0.009$ , see Table 2). Though, some data deviate from

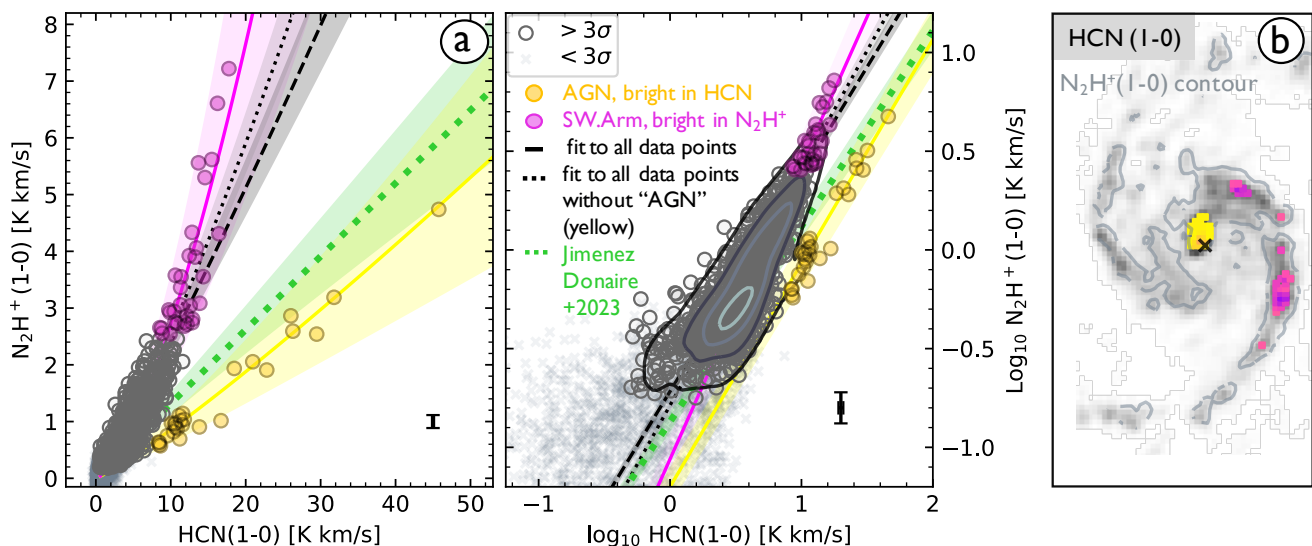


**Fig. 2.** a) Pixel-by-pixel distribution of integrated  $N_2H^+$  and HCN emission in linear (left panel) and logarithmic (right panel) scaling. Subsets of pixels are visually isolated based on their high  $N_2H^+$  (pink, SW.Arm) or HCN (yellow, AGN) values. Their location relative to the distribution of HCN emission in M51 is shown in b) (contour marks  $5\sigma$   $N_2H^+$  integrated intensity). Power-law fits are applied to all data points (black dashed line), the subsets identified (solid lines), as well as all data points excluding the yellow (AGN affected) subset (black dotted line). Fit parameters and Spearman correlation coefficients for all data points and the subsets are given in Table 2. Data points below the  $3\sigma$  noise level are presented as grey crosses. The  $N_2H^+$ -to-HCN relation from Jiménez-Donaire et al. (2023) is shown as a green dotted line.

**Table 2.** Fit parameters and Spearman correlation coefficients of  $N_2H^+$  as function of HCN

Region	Power $a$	Offset $b$	$\rho_{Sp}$	$p$ -value
All data	$1.10 \pm 0.02$	$-0.72 \pm 0.02$	$0.832 \pm 0.009$	$< 0.001$
All w/o AGN	$1.20 \pm 0.02$	$-0.79 \pm 0.02$	$0.834 \pm 0.009$	$< 0.001$
AGN, yellow	$1.13 \pm 0.04$	$-1.20 \pm 0.06$	$0.90 \pm 0.05$	$< 0.001$
SW.Arm, pink	$1.49 \pm 0.09$	$-1.06 \pm 0.10$	$0.75 \pm 0.05$	$< 0.001$

**Notes.** Fit parameters for a linear fit in log-log space ( $\log_{10} I_{N_2H^+} = a \cdot \log_{10} I_{HCN} + b$ ), which corresponds to a power-law relation in linear space ( $I_{N_2H^+} = 10^b \cdot I_{HCN}^a$ ). We add Spearman correlation coefficients  $\rho_{Sp}$  and corresponding  $p$ -values. We only consider pixels with significant emission (i.e.  $> 3\sigma$ ).

the correlation. The linear presentation (left panel) reveals two clusters with different mean slopes. We visually devise subsets of pixels that (a) belong to the main cluster containing the bulk of the data points (grey), (b) have comparably low  $N_2H^+$  flux while very high HCN fluxes (yellow), and (c) show the highest  $N_2H^+$  intensities where the apparently linear trend becomes exponential (pink). Locating these pixels in the HCN moment-0 map (Fig. 2 b) reveals that subset (b) originates from the galaxy center (yellow, hereafter "AGN") and subset (c) from the south-western arm (pink, hereafter "SW.Arm"). Pixels in the central part of the galaxy thus follow a distribution that is significantly fainter in  $N_2H^+$  emission than in HCN emission compared to the rest of the sample. We discuss the impact of the AGN in Section 4.1.

The logarithmic presentation (right panel of Fig. 2 a) confirms that subset (c, pink) from the south-western arm follows the bulk data (grey) for a power-law distribution. The comparably large scatter in this subset (c, SW.arm) emerges from two different spatial locations that have slightly different slopes than the subset's average one (see also Appendix E.1).

We fit all data points plus the subsets (emission  $> 3\sigma$ ) with linear functions in logarithmic scaling. Fit parameters as well

as Spearman correlation coefficients ( $\rho_{Sp}$ ) and  $p$ -values are provided in Table 2). Details on the fitting process, and the uncertainties derived via jackknifing are given in Appendix D. For all subsets,  $N_2H^+$  emission is similarly well ( $\rho_{Sp} > 0.75$ ) and super-linearly (best-fit power  $a > 1$ ) correlated with HCN emission. However, the fit of the central (yellow) data points significantly deviates from the fit for all data points including and excluding the central ones (black dashed and dotted line, see also Appendix D). The central subset contributes  $\sim 7\%$  of the total HCN and  $\sim 4\%$  of the total  $N_2H^+$  flux in our FoV, and contains most of the brightest HCN pixels. Although the disk data points (without AGN and SW.arm, grey points), can be best described with a linear relation (power  $a = 0.97 \pm 0.013$ ), the power index monotonically increases when the upper limit of the range in integrated  $N_2H^+$  emission used to select the fitted point is increased. This is likely due to the scatter around the power law decreasing at the same time as the data explores a larger part of the power law, increasing the range spanned by the data.

The  $N_2H^+$ -to- $^{12}CO$  and HCN-to- $^{12}CO$  distributions (Fig. C) behave similarly, as the central data points clearly deviate from the bulk distribution. Similar to the  $N_2H^+$ -to-HCN distribution, the  $N_2H^+$ -to- $^{12}CO$  distribution (Fig. C.1) is best described by a super-linear power-law, with its brightest end being mainly populated by the pixels from subset (c, SW.arm) (Table C.1). In contrast, the HCN-to- $^{12}CO$  distribution is best described by a sub-linear to linear power-law. We quantify the scatter of these distributions in Appendix E.2 and find that for all distributions, the scatter is of order  $\sim 0.14$  dex, while the total range covered by the lines cover  $\gtrsim 1.5$  dex.

### 3.4. Density-sensitive line ratio

The ratio of emission lines from HCN and  $^{12}CO$  ( $f = I_{HCN}/I_{CO}$ ) has been commonly used as an indication of the (average) gas density  $f_{dense}$  (e.g., Usero et al. 2015; Bigiel et al. 2016; Jiménez-Donaire et al. 2019). We compare  $I_{N_2H^+}/I_{CO}$  to  $f$  in Fig. 3



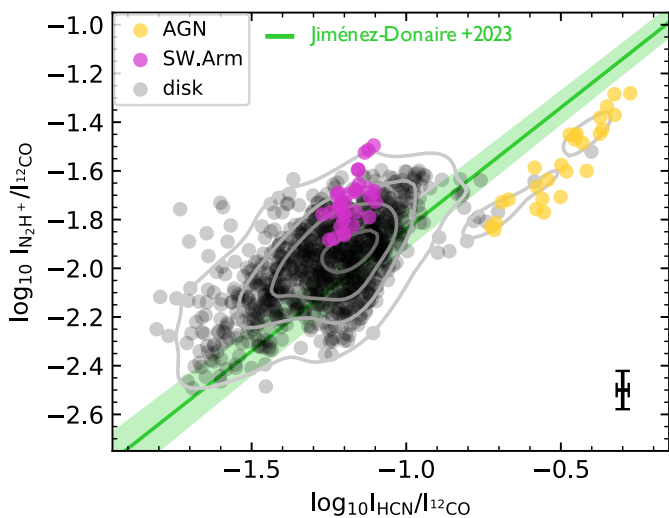


**Fig. 3.**  $I_{\text{N}_2\text{H}^+}/I_{\text{CO}}$  as function of  $I_{\text{HCN}}/I_{\text{CO}}$  for all data points and subsets above a  $3\sigma$  noise level. We show the average uncertainty in the bottom right corner, as well as the best-fit from Jimémez-Donaire et al. (2023, eq. 2) with a power law slope of 1.0 derived for extragalactic and Galactic data points (green line). Contours indicate the number density of data points.

and find them correlated ( $\rho_{\text{Sp}} = 0.70$ ,  $p$ -value  $< 0.001$ ). 82% (97%) of our data points agree within  $3\sigma$  ( $5\sigma$ ) with the fit from Jimémez-Donaire et al. (2023, eq. 2) with a power-law index of 1.0 obtained when fitting all available Galactic and extragalactic data (green line).

Our result indicates that, to first order, both line ratios are correlated. Although the difference has a low statistical significance, the AGN subset (b, yellow) is offset from the remaining data, and the  $\text{N}_2\text{H}^+$ -bright SW.arm subset (c, pink) clusters at higher  $\text{N}_2\text{H}^+/^{12}\text{CO}$  values.

#### 4. Discussion on molecular gas density in M 51

We discuss which physical conditions might impact the brightness of the potential dense molecular gas tracers based on the found distribution of  $\text{N}_2\text{H}^+$  and HCN in the disk (Sec. 3.1), the high/low line ratios in isolated regions (Sec. 3.2), and the correlations between emission of  $\text{N}_2\text{H}^+$  and HCN (Sec. 4.2).

##### 4.1. The AGN impacts the central emission in M 51

The  $\text{N}_2\text{H}^+$ -to-HCN line ratio is significantly lower in the center of M 51 compared to regions in the disk, and the central data points are offset from those in the disk (Fig. 2). In contrast, the HCN-to- $^{12}\text{CO}$  ratio is higher in the center compared to the remaining disk (compare Fig. C.1), in agreement with Jimémez-Donaire et al. (2019) at  $\sim$ kpc scales. Very high-resolution ( $\sim 30$  pc) observations of HCN and  $^{12}\text{CO}$  in M 51 by Matsushita et al. (2015) reveal extraordinarily high HCN/CO ratios ( $> 2$ ) at the location of the AGN, which they explain by infrared pumping, possibly weak HCN masing and an increased HCN abundance. Electron excitation in the XDR of the AGN might also contribute to the enhanced HCN emission (Goldsmith & Kauffmann 2017). Blanc et al. (2009) identified [NII] $\lambda 6584/\text{H}\alpha$  line ratios typical of AGN in M 51's central  $\sim 700$  pc spatially coincident with X-ray and radio emission. HCN and  $^{12}\text{CO}$  arise both from the outflow associated with nearly coplanar radio jet, with

significant effects seen out to 500 pc distance (Querejeta et al. 2016). While the central 1.5 kpc (diameter) region as used for the line ratios likely overestimates the area of influence of the AGN, our visually selected subset (b) likely underestimates the area impacted.

While both the HCN-to- $^{12}\text{CO}$  and the  $\text{N}_2\text{H}^+$ -to- $^{12}\text{CO}$  distribution (Fig. C.1) show an enhancement in HCN or  $\text{N}_2\text{H}^+$  emission in the central data points, the effect is less strong for  $\text{N}_2\text{H}^+$ -to- $^{12}\text{CO}$ , as the fit to its central points agrees with the disk fit unlike the HCN-to- $^{12}\text{CO}$  distribution (Appendix C). This implies that  $\text{N}_2\text{H}^+$  is less affected by the AGN than HCN. Galactic studies do not find correlations between  $\text{N}_2\text{H}^+$  and mid-infrared photons (e.g., Beuther et al. 2022) suggesting that  $\text{N}_2\text{H}^+$  is not affected by infrared-pumping via the AGN. While an increased temperature in the AGN vicinity can also increase HCN emission (Matsushita et al. 2015; Tafalla et al. 2023), this would lead to CO sublimating, reacting with and destroying  $\text{N}_2\text{H}^+$  in contrast to our findings. High cosmic ray ionization rates in the AGN surroundings might counter this effect by increasing the  $\text{N}_2\text{H}^+$  abundance (Santa-Maria et al. 2021), which is not seen for HCN (Meijerink et al. 2011). The complex mechanisms happening in the AGN vicinity will be explored in a future paper.

##### 4.2. The emerging $\text{N}_2\text{H}^+$ -to-HCN relation

Our global average  $\text{N}_2\text{H}^+$ -to-HCN ratio of  $0.20 \pm 0.09$  agrees well with ratios obtained at  $\sim$ kpc resolution in M 51 of  $\sim 0.14$  for the galaxy center, and  $\sim 0.19$  in the southern spiral arm (Watanabe et al. 2014; Aladro et al. 2015). A recent literature compilation (Jimémez-Donaire et al. 2023) finds that a  $\text{N}_2\text{H}^+$ -to-HCN ratio of  $0.07 - 0.22$  for extragalactic regions, and  $\sim 0.05 - 0.23$  when including Galactic sources. Line ratios of five  $\sim$ kpc size regions in NGC 6946 range between  $0.12 - 0.20$ , leading to a global ratio of  $0.15 \pm 0.03$ , or a linear fit in log-space of power  $0.99 \pm 0.04$  and offset  $0.87 \pm 0.04$  (Jimémez-Donaire et al. 2023) shown for references in Fig. 2. This fits agrees with our fit to the central subset (b), but shows a significant ( $> 3\sigma$ ) deviation from our fits focusing on the disk.

Given the AGN impact (Section 4.1), we consider the power-law fit without the central subset being most representative of typical conditions: The  $\text{N}_2\text{H}^+$  emission as a function of HCN emission in the disk at 125 pc can be described as:

$$\log_{10} I_{\text{N}_2\text{H}^+} = (1.20 \pm 0.02) \cdot \log_{10} I_{\text{HCN}} - (0.825 \pm 0.009) \quad (1)$$

The super-linearity in our relation, driving the discrepancy between our and the literature results, comes from the bright south-western spiral arm, where our  $\text{N}_2\text{H}^+$ -to-HCN ratio is the highest (Table 1, region 2). Strong streaming motions present in the southern spiral arm are likely stabilizing the gas resulting in low star formation efficiencies (Meidt et al. 2013). This region (at  $\sim 28 - 38''$ ) is at the transition between the normal star formation efficiency and the extremely low star formation efficiency seen further south (Querejeta et al. 2019) and has a high dynamical complexity (i.e., coinciding with the co-rotation radius of a  $m=3$  mode; Colombo et al. 2014). Although its  $\text{N}_2\text{H}^+$ -to-HCN ratio is larger than the global average, it extends the general distribution in a smooth manner (Fig. 2), unlike the clearly offset emission from M 51's center. We speculate the following:

a) HCN-bright regions have more dense gas (as traced by  $\text{N}_2\text{H}^+$ ) than what we would expect from the HCN intensities. This effect should potentially correlate with resolution, as higher-resolution observations able to resolve clouds would be able to better isolate the spatially smaller dense clumps.

b) Galactic studies find that HCN luminosity is sensitive to far-UV light from young massive stars (e.g., Pety et al. 2017; Kauffmann et al. 2017; Santa-Maria et al. 2023). HCN emission is linked to dense molecular clouds, but also well correlated with regions of recent star formation. This effect is not seen for  $\text{N}_2\text{H}^+$ , which is abundant in cold and dense regions where the depletion of CO onto dust grains inhibits the main route of  $\text{N}_2\text{H}^+$  destruction. In the southern-spiral arm, where star-formation is found to be comparably lower, this could explain our power law of 1.2.

As the focus of this study is the comparison of HCN to  $\text{N}_2\text{H}^+$  emission, we selected pixels in the disk where  $\text{N}_2\text{H}^+$  is detected. Since  $\text{N}_2\text{H}^+$  is a chemical tracer of dense gas, we thus selected regions where dense gas can be expected. This can introduce a bias towards higher values, as we potentially mask out regions of low  $\text{N}_2\text{H}^+$  emission.

## 5. Summary and Conclusion

We present the first map of  $\text{N}_2\text{H}^+$  ( $J=1-0$ ) and HCN ( $1-0$ ) from the NOEMA+30m large program SWAN in the central  $5 \times 7$  kpc of the nearby star-forming disk galaxy M 51 at cloud-scale resolution of 125 pc ( $3''$ ). We study where the chemical dense gas tracer  $\text{N}_2\text{H}^+$  emits with respect to larger-scale dynamical features and how it relates to emission from other molecules such as HCN and CO. Comparing these lines, we find the following:

1. Extended  $\text{N}_2\text{H}^+$  emission is detected from various regions across the disk, with the brightest emission found in the south-western spiral arm, followed by the center and the north-western end of the molecular ring. HCN emission is bright in the same regions, but it shows the highest intensity in the center.
2. We find an average  $\text{N}_2\text{H}^+$ -to-HCN ratio of  $0.20 \pm 0.09$  for regions detected in  $\text{N}_2\text{H}^+$  emission ( $> 3\sigma$ ) with strong variations throughout the disk of up to a factor of  $\sim 2 - 3$  in the south-western spiral arm and the center that hosts an AGN.  $\text{N}_2\text{H}^+$  and HCN emission are strongly correlated ( $\rho_{\text{Sp}} \sim 0.83$ ), but the central 1.5 kpc clearly deviates. The disk emission can be described with a super-linear power-law function of index  $1.20 \pm 0.02$ , indicating that HCN-bright regions have higher gas densities as traced by  $\text{N}_2\text{H}^+$  than we would infer from their HCN emission alone.
3. The  $\text{N}_2\text{H}^+$ -to-HCN ratio is significantly lower in the M 51's center where an AGN is present, and its distribution is offset from the bulk of the disk data. The affected region accounts for  $\sim 9\%$  of the total HCN emission and  $\sim 4\%$  of total  $\text{N}_2\text{H}^+$  emission in pixels in our FoV where  $\text{N}_2\text{H}^+$  is detected. Mid-IR pumping might be one explanation for the bright and enhanced HCN flux surrounding the AGN.

## References

Aladro, R., Martín, S., Riquelme, D., et al. 2015, *Astronomy & Astrophysics*, 579, A101, publisher: EDP Sciences  
 Barnes, A. T., Kauffmann, J., Bigiel, F., et al. 2020, *Monthly Notices of the Royal Astronomical Society*, 497, 1972  
 Bergin, E. A. & Tafalla, M. 2007, *Annual Review of Astronomy and Astrophysics*, 45, 339  
 Beuther, H., Wyrowski, F., Menten, K. M., et al. 2022, *Astronomy & Astrophysics*, 665, A63  
 Bešlić, I., Barnes, A. T., Bigiel, F., et al. 2021, *Monthly Notices of the Royal Astronomical Society*, 506, 963  
 Bigiel, F., Leroy, A., Walter, F., et al. 2008, *The Astronomical Journal*, 136, 2846  
 Bigiel, F., Leroy, A. K., Jiménez-Donaire, M. J., et al. 2016, *The Astrophysical Journal*, 822, L26  
 Blanc, G. A., Heiderman, A., Gebhardt, K., Evans, N. J., & Adams, J. 2009, *The Astrophysical Journal*, 704, 842

Chen, H., Braine, J., Gao, Y., Koda, J., & Gu, Q. 2017, *The Astrophysical Journal*, 836, 101  
 Colombo, D., Hughes, A., Schinnerer, E., et al. 2014, *The Astrophysical Journal*, 784, 3  
 den Brok, J. S., Bigiel, F., Sliwa, K., et al. 2022, *Astronomy & Astrophysics*, 662, A89  
 Dumas, G., Schinnerer, E., Tabatabaei, F. S., et al. 2011, *The Astronomical Journal*, 141, 41, publisher: The American Astronomical Society  
 Eibensteiner, C., Barnes, A. T., Bigiel, F., et al. 2022, *Astronomy & Astrophysics*, 659, A173  
 Einig, L., Pety, J., Roueff, A., et al. 2023, arXiv e-prints, arXiv:2307.13009  
 Gallagher, M. J., Leroy, A. K., Bigiel, F., et al. 2018, *The Astrophysical Journal*, 868, L38  
 Gao, Y. & Solomon, P. M. 2004, *The Astrophysical Journal*, 606, 271  
 Gildas Team. 2013, *Astrophysics Source Code Library*, ascl:1305.010, aDS Bibcode: 2013ascl.soft05010G  
 Goldsmith, P. F. & Kauffmann, J. 2017, *The Astrophysical Journal*, 841, 25  
 Helfer, T. T., Thornley, M. D., Regan, M. W., et al. 2003, *The Astrophysical Journal Supplement Series*, 145, 259  
 Ho, L. C., Filippenko, A. V., & Sargent, W. L. W. 1997, *The Astrophysical Journal Supplement Series*, 112, 315, publisher: IOP Publishing  
 Jiménez-Donaire, M. J., Bigiel, F., Leroy, A. K., et al. 2019, *The Astrophysical Journal*, 880, 127  
 Jiménez-Donaire, M. J., Usero, A., Bešlić, I., et al. 2023, *Astronomy & Astrophysics*, 676, L11, publisher: EDP Sciences  
 Kaneko, H., Tosaki, T., Tanaka, K., & Miyamoto, Y. 2023, *The Astrophysical Journal*, 953, 139, aDS Bibcode: 2023ApJ...953..139K  
 Kauffmann, J., Goldsmith, P. F., Melnick, G., et al. 2017, *Astronomy & Astrophysics*, 605, L5, arXiv:1707.05352 [astro-ph]  
 Kennicutt, R. C. & Evans, N. J. 2012, *Annual Review of Astronomy and Astrophysics*, 50, 531  
 Lada, C. J., Forbrich, J., Lombardi, M., & Alves, J. F. 2012, *The Astrophysical Journal*, 745, 190  
 Lada, C. J., Lombardi, M., & Alves, J. F. 2010, *The Astrophysical Journal*, 724, 687, publisher: The American Astronomical Society  
 Leroy, A. K., Hughes, A., Liu, D., et al. 2021, *The Astrophysical Journal Supplement Series*, 255, 19, publisher: The American Astronomical Society  
 Martín, S., Mangum, J. G., Harada, N., et al. 2021, *Astronomy & Astrophysics*, 656, A46, publisher: EDP Sciences  
 Matsushita, S., Trung, D.-V., Boone, F., et al. 2015, *The Astrophysical Journal*, 799, 26, publisher: The American Astronomical Society  
 McQuinn, K. B. W., Skillman, E. D., Dolphin, A. E., Berg, D., & Kennicutt, R. 2016, *The Astrophysical Journal*, 826, 21, publisher: The American Astronomical Society  
 Meidt, S. E., Schinnerer, E., García-Burillo, S., et al. 2013, *The Astrophysical Journal*, 779, 45  
 Meijerink, R., Spaans, M., Loenen, A. F., & Werf, P. P. v. d. 2011, *Astronomy & Astrophysics*, 525, A119, publisher: EDP Sciences  
 Neumann, L., Gallagher, M. J., Bigiel, F., et al. 2023, *Monthly Notices of the Royal Astronomical Society*, 521, 3348  
 Pety, J., Guzmán, V. V., Orkisz, J. H., et al. 2017, *Astronomy & Astrophysics*, 599, A98  
 Pety, J. & Rodríguez-Fernández, N. 2010, *A&A*, 517, A12  
 Querejeta, M., Schinnerer, E., García-Burillo, S., et al. 2016, *Astronomy & Astrophysics*, 593, A118, arXiv: 1607.00010  
 Querejeta, M., Schinnerer, E., Schruha, A., et al. 2019, *Astronomy & Astrophysics*, 625, A19  
 Santa-Maria, M. G., Goicoechea, J. R., Etxaluze, M., Cernicharo, J., & Cuadrado, S. 2021, *Astronomy & Astrophysics*, 649, A32  
 Santa-Maria, M. G., Goicoechea, J. R., Pety, J., et al. 2023, publication Title: arXiv e-prints ADS Bibcode: 2023arXiv230903186S  
 Schinnerer, E., Meidt, S. E., Pety, J., et al. 2013, *The Astrophysical Journal*, 779, 42  
 Shetty, R., Vogel, S. N., Ostriker, E. C., & Teuben, P. J. 2007, *The Astrophysical Journal*, 665, 1138, publisher: IOP Publishing  
 Shirley, Y. L. 2015, *Publications of the Astronomical Society of the Pacific*, 127, 299  
 Tafalla, M., Usero, A., & Hacar, A. 2021, *Astronomy & Astrophysics*, 646, A97, arXiv:2101.02710 [astro-ph]  
 Tafalla, M., Usero, A., & Hacar, A. 2023, arXiv:2309.14414 [astro-ph]  
 Tatematsu, K., Kandori, R., Umemoto, T., & Sekimoto, Y. 2008, *Publications of the Astronomical Society of Japan*, 60, 407, arXiv:0804.0111 [astro-ph]  
 Usero, A., Leroy, A. K., Walter, F., et al. 2015, *The Astronomical Journal*, 150, 115  
 Virtanen, P., Gommers, R., Oliphant, T. E., et al. 2020, *Nature Methods*, 17, 261, number: 3 Publisher: Nature Publishing Group  
 Watanabe, Y., Sakai, N., Sorai, K., & Yamamoto, S. 2014, *The Astrophysical Journal*, 788, 4, publisher: The American Astronomical Society

- <sup>1</sup> Max-Planck-Institut für Astronomie, Königstuhl 17, 69117 Heidelberg Germany
- <sup>2</sup> IRAM, 300 rue de la Piscine, 38400 Saint Martin d’Hères, France
- <sup>3</sup> Sorbonne Université, Observatoire de Paris, Université PSL, École normale supérieure, CNRS, LERMA, F-75005, Paris, France
- <sup>4</sup> Argelander-Institut für Astronomie, Universität Bonn, Auf dem Hügel 71, 53121 Bonn, Germany
- <sup>5</sup> Observatorio Astronómico Nacional (IGN), C/Alfonso XII 3, Madrid E-28014, Spain
- <sup>6</sup> Centro de Desarrollos Tecnológicos, Observatorio de Yebes (IGN), 19141 Yebes, Guadalajara, Spain
- <sup>7</sup> Department of Astronomy, The Ohio State University, 140 West 18th Ave, Columbus, OH 43210, USA
- <sup>8</sup> Center for Astrophysics | Harvard & Smithsonian, 60 Garden St., 02138 Cambridge, MA, USA
- <sup>9</sup> Center for Astrophysics and Space Sciences, University of California San Diego, 9500 Gilman Drive, La Jolla, CA 92093, USA
- <sup>10</sup> European Southern Observatory, Karl-Schwarzschild 2, 85748 Garching bei Muenchen, Germany
- <sup>11</sup> Institut für Theoretische Astrophysik, Zentrum für Astronomie der Universität Heidelberg, Albert- Ueberle-Strasse 2, 69120 Heidelberg, Germany
- <sup>12</sup> Cosmic Origins Of Life (COOL) Research DAO, coolresearch.io
- <sup>13</sup> Department of Physics & Astronomy, University of Wyoming, Laramie, WY 82071, USA
- <sup>14</sup> Max-Planck-Institut für extraterrestrische Physik, Giessenbachstraße 1, D-85748 Garching, Germany
- <sup>15</sup> Department of Physics, Tamkang University, No.151, Yingzhuang Road, Tamsui District, New Taipei City 251301, Taiwan

*Acknowledgements.* This work was carried out as part of the PHANGS collaboration. We thank the anonymous referee for their constructive feedback. This work is based on data obtained by PIs E.Schinnerer and F.Bigiel with the IRAM-30m telescope and NOEMA observatory under project ID M19AA. SKS acknowledges financial support from the German Research Foundation (DFG) via Sino-German research grant SCHI 536/11-1. JP acknowledges support from the French Agence Nationale de la Recherche through the DAOISM grant ANR-21-CE31-0010 and from the Programme National “Physique et Chimie du Milieu Interstellaire” (PCMI) of CNRS/INSU with INC/INP co-funded by CEA and CNES. ES acknowledges funding from the European Research Council (ERC) under the European Union’s Horizon 2020 research and innovation programme (grant agreement No. 694343). AU acknowledges support from the Spanish grant PID2019-108765GB-I00, funded by MCIN/AEI/10.13039/501100011033. MQ and MJJD acknowledge support from the Spanish grant PID2019-106027GA-C44, funded by MCIN/AEI/10.13039/501100011033. JdB acknowledges support from the Smithsonian Institution as a Submillimeter Array (SMA) Fellow. LN acknowledges funding from the Deutsche Forschungsgemeinschaft (DFG, German Research Foundation) - 516405419. The work of AKL is partially supported by the National Science Foundation under Grants No. 1615105, 1615109, and 1653300. CE acknowledges funding from the Deutsche Forschungsgemeinschaft (DFG) Sachbeihilfe, grant number BI1546/3-1. Y-HT acknowledges funding support from NRAO Student Observing Support Grant SOSPADA-012 and from the National Science Foundation (NSF) under grant No. 2108081. MC gratefully acknowledges funding from the Deutsche Forschungsgemeinschaft (DFG) through an Emmy Noether Research Group, grant number CH2137/1-1. COOL Research DAO is a Decentralized Autonomous Organization supporting research in astrophysics aimed at uncovering our cosmic origins. SCOG acknowledges support from the DFG via SFB 881 “The Milky Way System” (sub-projects B1, B2 and B8) and from the Heidelberg cluster of excellence EXC 2181-390900948 “STRUCTURES: A unifying approach to emergent phenomena in the physical world, mathematics, and complex data”, funded by the German Excellence Strategy. HAP acknowledges support by the National Science and Technology Council of Taiwan under grant 110-2112-M-032-020-MY3.

## Appendix A: Data

We utilize observations from the IRAM large program LP003 (PIs: E. Schinnerer, F. Bigiel) that used the Northern Extended Millimetre Array (NOEMA) and 30m single dish to map the 4-3 mm line emission from the central  $5 \times 7$  kpc of the nearby galaxy M 51. The observations, data calibration and imaging resulting in our final datasets are briefly described below.

### Appendix A.1: NOEMA data

NOEMA observations were taken with 9-11 antennas between January 2020 and December 2021, resulting in a total of 214 hours under average to excellent observing conditions with an average water vapor of  $\sim 4$  mm split across C (59%; 126h) and D (41%; 88h) configuration. Observations of the phase and amplitude calibrators (J1259+516 and J1332+473, replaced by 1418+546 if one of the two was not available) were executed every  $\sim 20$  minutes. The mosaic consists of 17 pointings in a hexagonal grid. Data reduction was carried out using the IRAM standard calibration pipeline in GILDAS (Gildas Team 2013). Average to excellent temporal subsets of the observed data were selected based on the relative seeing of the different tracks. Absolute flux calibration was done using IRAM models for MWC349 and LkHa101 providing about 50 independent measurements of the flux of J1259+516 and J1332+473 over a period of about 1 year. This allowed us to confirm that the time variations of the flux of these quasars were relatively smooth.

We detect emission from 9 molecular lines between  $\sim 80$  and 110 GHz, including HCN(1–0; 88.6 GHz) and  $\text{N}_2\text{H}^+$  (1–0; 93 GHz) presented in this paper, but also  $\text{C}_2\text{H}$ (1–0), HNC(4–3),  $\text{HCO}^+$ (1–0), HNC(1–0),  $\text{C}^{18}\text{O}$ (1–0), HNC(5–4) and  $^{13}\text{CO}$ (1–0). Continuum was subtracted from the  $uv$  visibilities by fitting a baseline of order 0 for each visibility, excluding channels in a velocity range of 300 km/s around the redshifted-frequency of each line. For each line, the NOEMA data were resampled to a spectral axis with 10 km/s resolution, relative to the systemic velocity of  $v_{\text{sys}} = 471.7$  km/s (Shetty et al. 2007).

### Appendix A.2: IRAM-30m single-dish data

In order to sample all the spatial scales, we need to combine the NOEMA interferometric imaging with single dish data of the HCN(1–0) and  $\text{N}_2\text{H}^+$  (1–0) emission lines from both archival and new observations.

The HCN(1–0) emission line was observed as part of the IRAM-30m survey EMPIRE (Jiménez-Donaire et al. 2019), using the 3 mm band (E090) of the dual-polarization EMIR receiver (Carter et al. 2012).  $\text{N}_2\text{H}^+$  (1–0) was observed by the IRAM-30m CLAWS survey (055-17, PI: K. Sliwa; den Brok et al. 2022), where EMIR was also used to map the 1 mm (220 GHz) and 3 mm (100 GHz) emission lines in M 51. In both surveys, the integration time was spread over the full extent of M 51, while the required field-of-view (FoV) for the 30m imaging is the interferometric FoV plus a guard-band to avoid edge effects amounting to 5 square arcmin. We estimate that the EMPIRE and CLAWS projects obtained each about 14 hours of 30m integration time over the relevant field of view. As a rule of thumb to achieve an optimum combination one needs to observe with the 30m telescope the same amount of time as is spent in the compact D configuration<sup>3</sup>. Hence we obtained 55 hours of

additional IRAM 30m observations (project 19-238 observed in February and April 2020) with a similar tuning as the NOEMA one. In all three cases, we used the on-the-fly/position switching (OTF-PSW) mode, with emission-free reference positions close to the galaxy. The fast Fourier transform spectrometers (FTS) were used to record the data. We refer to Jiménez-Donaire et al. (2019) and den Brok et al. (2022) for details of the observations.

The data were (re)-reduced (1) to ensure a homogeneous treatment, and (2) to avoid unnecessary spatial or spectral re-gridding. In short, for each observed spectrum, we first extracted a frequency range of 300 MHz centered on each target line. We then converted the temperature scale from  $T_A^*$  to  $T_{\text{mb}}$  by applying the relevant Ruze formula with the CLASS command `MODIFY BEAM_EFF /RUZE`. We computed the velocity scale corresponding to each line's redshifted velocity, and we reprojected the spatial offsets of each observed spectrum to the NOEMA projection center of RA=13:29:52.532, Dec=47:11:41.982. We also subtracted an order 1 polynomial baseline fitted excluding a velocity range of  $[-170, +170]$  km/s. We finally gridded all the data on the same spatial and spectral grid as the NOEMA data. The achieved noise levels are 2.5 K at 29.3'' and 2.4 K at 27.9'' for the HCN and  $\text{N}_2\text{H}^+$  (1–0) lines, respectively.

### Appendix A.3: NOEMA+30m imaging

The 30m data are then merged with the NOEMA data in the  $uv$  plane using the GILDAS `UV_SHORT` command (see Pety & Rodríguez-Fernández 2010, for details). The combined data are imaged with `UV_MAP` on a grid of  $768 \times 1024$  pixels of 0.31'' size. Högbom-cleaning without cleaning mask was run in order to achieve residuals consistent with a Gaussian distribution of the noise. In practice, we ran it until a stable number of clean components, which depends on the line, was reached. The intensity scale was finally converted from Jy/beam to K. The resulting dataset has a rms of  $\sim 20$  mK per 10 km/s channel at a nominal resolution of  $2.1 \times 2.4''$  for the brightest line,  $^{13}\text{CO}$ (1–0).

We created the following sets of integrated moment-0 maps for the NOEMA+30m HCN and  $\text{N}_2\text{H}^+$  datacubes as well as for the  $^{12}\text{CO}$ (J = 1–0) data from PAWS (Schinnerer et al. 2013). All data are convolved to a common angular and spectral resolution of 3'' (125 pc) and 10 km/s per channel. We integrated each line by applying the so-called *island-method* based on  $^{12}\text{CO}$  emission (see Einig et al. 2023, and reference therein). This method isolates connected structures with  $^{12}\text{CO}$  emission above our selected S/N threshold of 2 in the position-position-velocity (*ppv*) cube and integrates the emission of selected lines over the identified structures along the velocity axis. To avoid misleading oversampling effects, we regrid our maps to pixels with sizes of half the beam major axis for all calculations (i.e. 1.5''). Using  $^{12}\text{CO}$  emission to detect the *islands* ensures that for all lines the same pixels in the *ppv* cube are used for integration. Since  $^{12}\text{CO}$  is brighter than the other lines, there are more pixels above a given S/N threshold than in  $\text{N}_2\text{H}^+$  and HCN. Therefore, this can result in otherwise too faint emission being stacked in pixels that would not be selected for integration based on, e.g.,  $\text{N}_2\text{H}^+$  emission.

For comparison, we also integrate each line individually, by selecting *islands* based on each line's intensity. This reduces the noise for each line individually while conserving faint emission from connected structures. However, this also introduces some bias, as emission is integrated over a varying amount of pixels in different structures for each line. While some values slightly change due to these effects, we confirmed that all trends and conclusions remain unchanged.

<sup>3</sup>See the IRAM technical memo IRAM-2008-2, <https://cloud.iram.fr/index.php/s/Ney5P2BeN7DAEWX>



Pixels where the  $N_2H^+$  integrated emission is significantly ( $>3\sigma$ ) detected, contain  $\sim 50\%$  of significant  $^{12}CO$  flux in our FoV and  $\sim 70\%$  of significant HCN emission in the FoV. Pixels where HCN is significantly detected contain  $\sim 90\%$  of the significant  $^{12}CO$  emission in our FoV. Since the our analysis in section 3 is based on regions where  $N_2H^+$  is detected, we limit our analysis to a smaller area in the FoV.

## Appendix B: Typical cloud mass per beam

As  $N_2H^+$  is abundant in small dense cores, we generally expect the  $N_2H^+$  emission to arise from regions with sizes much smaller than our resolution of 125 pc, which is slightly worse than the size of massive GMCs. Thus, the pixel-by-pixel variations in our observations reflect average physical trends affecting ensembles of multiple clumps. Our finding in Sec. 3.1, that linewidths of  $N_2H^+$  are comparable to HCN in selected beam-size regions, suggests that at our 125 pc scales we are indeed averaging emission from several dense clouds. This is further supported by the typical emission found in these regions. In the selected beam-size regions (see Fig. 1), we find typical integrated  $^{12}CO$  intensities of  $I_{CO} \sim 1 \times 10^2$  K km/s. A typical large molecular cloud with cloud masses of  $M_{cloud} \sim 1 \times 10^5 M_\odot$  would at our resolution correspond to integrated intensities of 1.3 K km/s using a standard CO-to- $H_2$  conversion factor of  $\alpha_{CO} = 4.35 M_\odot pc^{-2} (K km/s)^{-1}$ . Therefore we can confirm that at our resolution we are likely averaging emission from several clouds.

## Appendix C: The $N_2H^+$ -to- $^{12}CO$ and HCN-to- $^{12}CO$ relation

In addition to the  $N_2H^+$ -to-HCN distribution (Fig. 2), we show the  $N_2H^+$ -to- $^{12}CO$  and HCN-to- $^{12}CO$  distributions in Fig. C.1. We mark the same subset of pixels (AGN, SW.arm) identified in the  $N_2H^+$ -to-HCN distribution accordingly. We fit power-laws to all the data (dashed line), the data without the central points (dotted line), as well as the subsets of data (subset (b) AGN, subset (c) SW.arm). Fit parameters can be found in Table C.1 and more details on the fitting process are provided in Appendix D. Similarly to our previous findings, we see that the central data points follow a steeper trend than the rest of the data points. While the central points in the HCN-to- $^{12}CO$  distribution do not overlap with the rest of the data, the central  $N_2H^+$ -to- $^{12}CO$  distribution mostly overlaps with the rest of the data points and the central  $N_2H^+$ -to- $^{12}CO$  trend is only slightly steeper than the global trend.

The  $N_2H^+$ -bright data points from the southern spiral arm (subset (c): pink) are also the brightest pixels in  $^{12}CO$ . These points constitute a super-linear relation in the  $N_2H^+$ -to- $^{12}CO$  plane. This is less clear for the HCN-to- $^{12}CO$  distribution. While all fits to the  $N_2H^+$ -to- $^{12}CO$  data and subsets are super-linear ( $a > 1$ ), all fits to the HCN-to- $^{12}CO$  data and subsets are sub-linear ( $a < 1$ ) except for the fit to subset (c). We note, however, that there are additional data points in the HCN-to- $^{12}CO$  distribution, which are elevated above the bulk distribution that might instead belong to the central subset (b), but are not selected since our selection of these subsets is visually determined based on the  $N_2H^+$ -to-HCN distribution. While the fit to all data points shows a large increase in offset due to the central data points, the fit without the central subset might still be elevated due to the likely imperfect selection of data points impacted by the AGN.

The fit to the central subset (b) of the HCN-to- $^{12}CO$  distribution significantly deviates from the fit to the disk data without

**Table C.1.** Power-law fit parameters of  $N_2H^+$  as a function of  $^{12}CO$ , and HCN as a function of  $^{12}CO$

Region	Power $a$	Offset $b$	$\rho_{Sp}$	$p$ -value
<b><math>N_2H^+</math>-to-<math>^{12}CO</math></b>				
All data	$1.12 \pm 0.02$	$-2.05 \pm 0.04$	$0.692 \pm 0.007$	$<0.001$
All w/o AGN	$1.19 \pm 0.03$	$-2.19 \pm 0.05$	$0.751 \pm 0.005$	$<0.001$
AGN, yellow	$1.23 \pm 0.07$	$-1.86 \pm 0.12$	$0.69 \pm 0.03$	$<0.001$
SW.Arm, pink	$1.53 \pm 0.14$	$-2.89 \pm 0.32$	$0.82 \pm 0.02$	$<0.001$
<b>HCN-to-<math>^{12}CO</math></b>				
All data	$0.50 \pm 0.02$	$-0.15 \pm 0.04$	$0.836 \pm 0.003$	$<0.001$
All w/o AGN	$0.86 \pm 0.01$	$-0.90 \pm 0.01$	$0.844 \pm 0.003$	$<0.001$
AGN, yellow	$0.91 \pm 0.05$	$-0.35 \pm 0.08$	$0.68 \pm 0.03$	$<0.001$
SW.Arm, pink	$1.01 \pm 0.05$	$-1.18 \pm 0.11$	$0.82 \pm 0.02$	$<0.001$

**Notes.** Fit parameters and spearman correlation coefficients according to a linear fit in log-log space similar to Table 2 but for the  $N_2H^+$ -to- $^{12}CO$  and HCN-to- $^{12}CO$  distribution.

this subset, similar to our findings for the  $N_2H^+$ -to-HCN distribution. Unsurprisingly, this is not the case for the central fit of the  $N_2H^+$ -to- $^{12}CO$  distribution, which agrees well with the fit to the disk data, as most of the central subset (b) overlaps with the disk data. This indicates that the mechanism driving the offset in line emission affects  $N_2H^+$  less than HCN (see discussion in Section 4).

## Appendix D: Fitting the $N_2H^+$ -to-HCN, $N_2H^+$ -to- $^{12}CO$ and HCN-to- $^{12}CO$ distribution

We fit all data points, the data subsets (b,c) as well as all disk data (all data without subset (b) AGN) of the  $N_2H^+$ -to-HCN,  $N_2H^+$ -to- $^{12}CO$  and HCN-to- $^{12}CO$  distributions with linear functions in logarithmic scaling. We only consider pixels with significant emission ( $> 3\sigma$ ). Parameters are fitted with `curve_fit` (python `scipy-optimize` tool; Virtanen et al. 2020). We fit a linear function of shape  $f(x) = ax + b$  to the logarithmic data with slope  $a$  and offset  $b$ . Following error propagation, the corresponding uncertainty at each  $x$  value is  $\Delta f(x) = \sqrt{(\Delta ax)^2 + (\Delta b)^2}$ , with uncertainties  $\Delta a$ ,  $\Delta b$  accordingly. The discrepancy to the literature fit is measured as  $\sigma = |f - f_{lit}| / \sqrt{\Delta f^2 + \Delta f_{lit}^2}$ , which is dependent on  $x$ . We provide the average discrepancy in the range over which our data are measured.

Uncertainties are estimated by perturbing each pixel by a random Gaussian value with standard deviation at the corresponding noise value, and randomly jackknifing 10% of the data before either calculating fit-parameters or Spearman correlation coefficients. Repeating this 100 times yields the standard deviation as uncertainty.

## Appendix E: Quantifying the scatter of line ratios

We investigate regions with increased scatter, as well as quantify the scatter between  $N_2H^+$  and HCN, HCN and  $^{12}CO$  as well as  $N_2H^+$  and  $^{12}CO$ .

### Appendix E.1: Disentangling emission from the southern spiral arm

In Sec. 4.2 we isolated pixels that are bright in HCN and  $N_2H^+$ . The region with pixels brightest in  $N_2H^+$  (subset (c): pink points in Fig. 2) shows a comparably large scatter in  $N_2H^+$  emission,

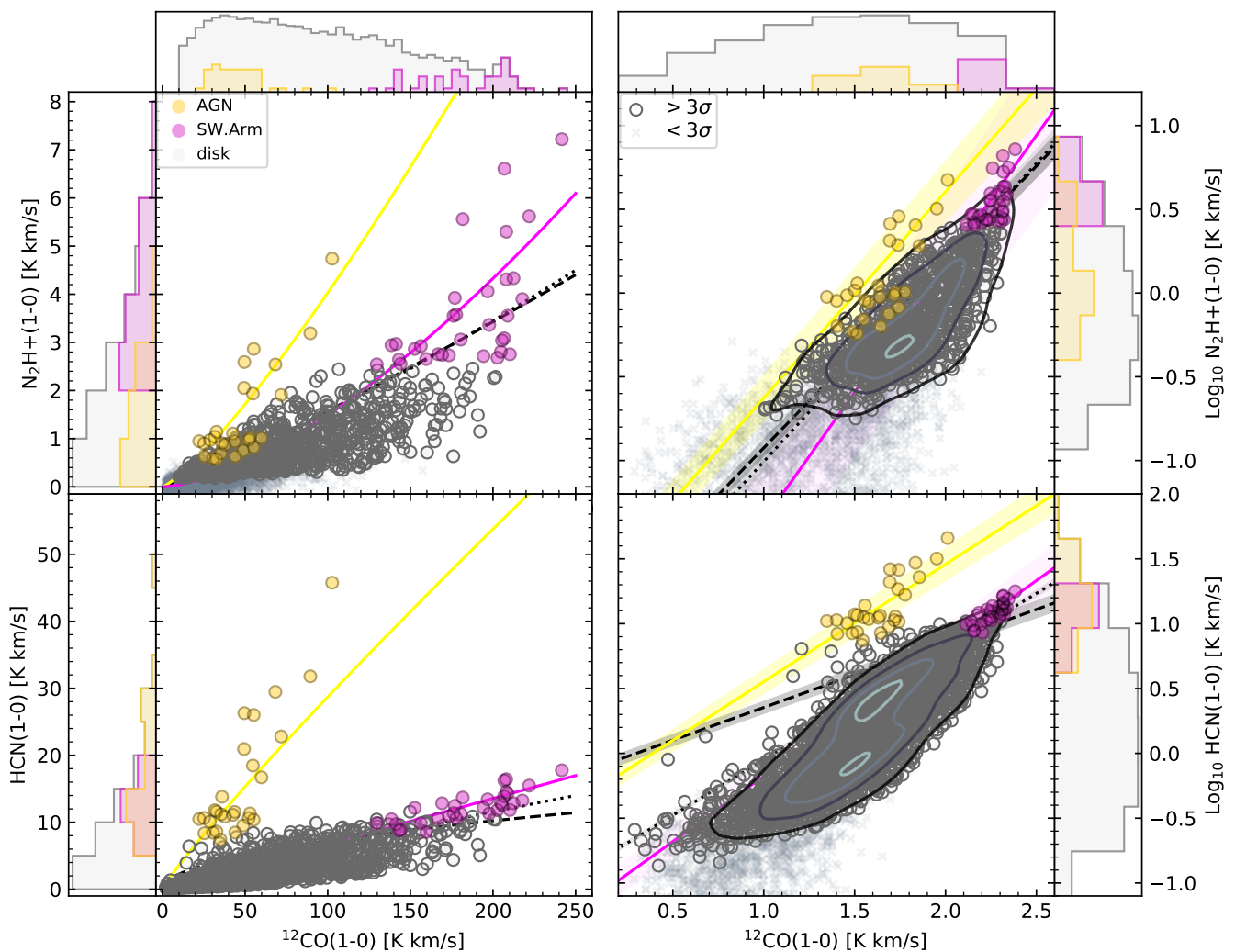


**Fig. C.1.** Pixel-by-pixel distribution of integrated  $\text{N}_2\text{H}^+$  (top panels) and HCN (bottom panels) as function of  $^{12}\text{CO}$  emission, similar to Fig. 2 (a) in linear (left panels) and logarithmic (right panels) scaling. Subsets of pixels isolated in Fig. 2 are marked accordingly (pink: subset (c) SW.Arm, yellow: Subset (b) AGN). Power-law fits to the full data (black dashed), the data without the central points (black dotted) and the subsets are added (colors respectively). Fit uncertainties are only shown in log space to ease visibility.

with the emission varying by nearly a factor of 2 at similar levels of HCN flux (at  $I_{\text{HCN}} \sim 18$  K km/s we find  $I_{\text{N}_2\text{H}^+} \sim 4 - 7.5$  K km/s). A closer look (Fig. E.1) reveals that this emission originates from different spatial locations in the disk, one with a shallower  $\text{N}_2\text{H}^+$ -to-HCN distribution located in the north-western part of the molecular ring (pink circles), the other with a steeper  $\text{N}_2\text{H}^+$ -to-HCN distribution from the south-western part of the same spiral arm (dark red circles).

As noted in Sec. 4.2, the data points from the southern spiral arm (red points in Fig. E.1) drive the non-linear but logarithmic relation between  $\text{N}_2\text{H}^+$  and HCN emission. Interestingly, the northern region is located close to the AGN jet major axis (Querejeta et al. 2016), and might be potentially impacted by the AGN as well, though the number of data points is lower.

#### Appendix E.2: Measuring the scatter of line ratios

We quantify the scatter of the  $\text{N}_2\text{H}^+$ -to-HCN, HCN-to- $^{12}\text{CO}$  and the  $\text{N}_2\text{H}^+$ -to-HCN distribution as follows: For this analysis, we exclude the central subset (b) that exhibits a quite different distribution from the rest of the data, as well as data points below

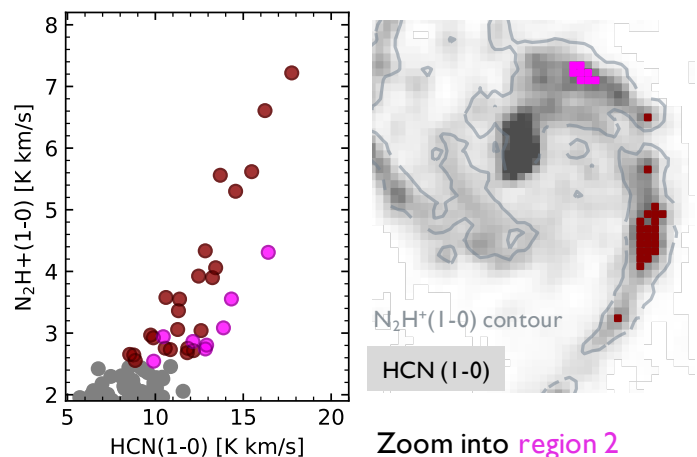


**Fig. E.1.** Close-up of HCN and  $\text{N}_2\text{H}^+$  emission (left panel) of  $\text{N}_2\text{H}^+$ -bright pixels (subset (c), see Fig. 2), as well as their location in the disk (right panel, compare to panel b of Fig. 2). We separate the pixels into two sub-regions (red, pink)

the  $3\sigma$  noise level. We subtract the corresponding best-fit value (using the fit parameters when excluding the center) from each data point in the according distribution. The obtained data has an average scatter of  $\sim 0.14$  dex for  $\text{N}_2\text{H}^+$  as a function of HCN emission,  $0.19$  dex for  $\text{N}_2\text{H}^+$  as a function of  $^{12}\text{CO}$  emission and  $0.29$  dex for HCN as a function of  $^{12}\text{CO}$  emission.

We conclude the following: a) While all lines span a range of  $\gtrsim 1.5$  dex in intensity, we find  $\sim 10\%$  scatter, indicating that all lines are well correlated. b) The scatter of  $\text{N}_2\text{H}^+$  as a function of HCN is least, indicating a tighter correlation between  $\text{N}_2\text{H}^+$  and HCN than any of those lines with  $^{12}\text{CO}$ . Since these results are strongly dependent on the fit and thus the fitting tool used, we suggest that the reader should take these results with caution.